TURUN YLIOPISTO
UNIVERSITY OF TURKU

MRI-ONLY RADIOTHERAPY TREATMENT PLANNING OF THE BRAIN

Iiro Ranta

MRI-ONLY RADIOTHERAPY TREATMENT PLANNING OF THE BRAIN

Iiro Ranta

University of Turku

Faculty of Science
Department of Physics and Astronomy
Medical Physics
Doctoral Programme in Clinical Research (DPCR)

Supervised by

Adjunct Professor Jani Keyriläinen
Department of Medical Physics
Turku University Hospital
Turku, Finland

Adjunct Professor Mika Kapanen
Department of Medical Physics
Tampere University Hospital
Tampere, Finland

Reviewed by

Adjunct Professor Aki Kangasmäki
Department of Physics
University of Helsinki
Helsinki, Finland

Assistant Professor Leonard Wee
Clinical Data Science
Maastro Clinic
Maastricht, The Netherlands

Opponent

Adjunct Professor Juha Nikkinen
Research Unit of Medical Imaging
Physics and Technology
University of Oulu
Oulu, Finland

UNIVERSITY OF TURKU
Faculty of Science
Department of Physics and Astronomy
Medical Physics
IIRO RANTA: MRI-only Radiotherapy Treatment Planning of the Brain
Doctoral Dissertation, 97 pp.
Doctoral Programme in Clinical Research
February 2023

ABSTRACT

Advancements in imaging methods have made it possible to create synthetic computed tomography (sCT) images from magnetic resonance imaging (MRI) data. MRI-based methods enable computed tomography (CT) to be omitted from the radiotherapy (RT) workflow and transitioning into MRI-only radiotherapy planning (RTP) of the brain. Geometric distortions in magnetic resonance (MR) images and the resulting image quality of generated sCTs are a challenge for the accuracy requirements of RT compared with CT-based methods of RTP.

The current dissertation evaluated the suitability of the latest MRI scanners for MRI-only RTP, and the clinical feasibility of present quality assurance methods for measuring geometric accuracy. The clinical feasibility of MRI-only brain RTP of two different sCT generation methods was also investigated. The magnetic resonance attenuation correction (MRAC) based sCT generation method was evaluated for dosimetric accuracy. Additionally, the clinical feasibility of a commercially available deep learning based sCT generation algorithm was evaluated in terms of dosimetric and patient positioning accuracy.

Based on the results of the current dissertation, the geometric accuracy of state-of-the-art MRI scanners were shown to meet the requirements of MRI-only based brain RTP. The results also showed that the sCT images generated by the MRAC method are useful for performing dose calculation in the brain. The sCTs generated using a commercial method demonstrated clinical feasibility of dose calculation and patient positioning for MRI-only brain RTP.

KEYWORDS: magnetic resonance imaging, radiotherapy, radiotherapy treatment planning, geometric distortion, synthetic computed tomography

TURUN YLIOPISTO
Matemaattis-luonnontieteellinen tiedekunta
Fysiikan ja tähtitieteen laitos
Lääketieteellinen fysiikka
IIRO RANTA: Magneettikuvauspohjainen sädehoidon suunnittelu aivojen
alueella
Väitöskirja, 97 s.
Turun Kliininen Tohtoriohjelma
Helmikuu 2023

TIIVISTELMÄ

Kuvantamismenetelmien kehitys on mahdollistanut pelkästään magneettikuvauksesta (MK) saatavaan informaatioon perustuen ns. synteettisten tietokonetomografiakuvien (sTT) muodostamisen aivojen alueella. MK-pohjaisten menetelmien avulla on mahdollista luopua kokonaan tietokonetomografiasta (TT) osana sädehoidon suunnitteluketjua ja siirtyä aivojen alueella kokonaan MK-pohjaiseen sädehoidon suunnitteluun. Magneettikuvissa esiintyvät geometriset vääristymät, sekä niiden pohjalta muodostettavien sTT-kuvien laatu ovat mahdollinen haaste sädehoidon tarkkuusvaatimusten kannalta verrattuna TT-kuvaukseen pohjautuviin menetelmiin.

Tässä väitöstutkimuksessa arvioitiin nykyisin käytössä olevien MK-laitteiden soveltuvuutta MK-pohjaiseen sädehoidon suunnitteluun, ja nykyisin käytössä olevien geometrisen tarkkuuden laadunvarmistusmenetelmien soveltuvuutta kliiniseen laadunvalvontaan sädehoidossa. MK-pohjaisen sädehoidon suunnittelun kliinistä soveltuvuutta aivojen alueelle tutkittiin kahdella eri menetelmällä. MK-pohjaiseen vaimennuskorjausmenetelmään perustuvan sTT-generointimallin soveltuvuutta arvioitiin annoslaskennan tarkkuuden osalta. Lisäksi tutkittiin kaupallisen, syväoppimiseen pohjautuvan algoritmin tuottamien sTT-kuvien soveltuvuutta kliiniseen käyttöön annoslaskennan ja potilasasettelun verifioinnin tarkkuuden osalta.

Väitöstutkimuksen tulosten perusteella voitiin osoittaa, että nykyaikaiset MK-laitteet täyttävät geometrisen tarkkuuden osalta vaatimukset MK-pohjaiseen sädehoidon suunnittelukuvantamiseen pään alueella. Lisäksi tulokset osoittivat, että MK-pohjaiseen vaimennuskorjaukseen pohjautuvalla menetelmällä luodut sTT-kuvat soveltuvat sädehoidon annoslaskennan toteuttamiseen aivojen alueella. Kaupallisella menetelmällä luodut sTT-kuvat voitiin todeta soveltuviksi kliiniseen käyttöön sädehoidon suunnittelussa aivojen alueella annoslaskennan ja potilasasettelun verifioinnin tarkkuuden osalta.

ASIASANAT: magneettikuvantaminen, sädehoito, sädehoidon suunnittelu, geometrinen vääristymä, synteettinen tietokonetomografia

Acknowledgements

Table of Contents

List of Original Publications

This dissertation is based on the following original publications, which are referred to in the text with Roman numerals:

I   Ranta I, Kemppainen R, Keyriläinen J, Suilamo S, Heikkinen S, Kapanen M, Saunavaara J. Quality Assurance Measurements of Geometric Accuracy for Magnetic Resonance Imaging-based Radiotherapy Treatment Planning. *Physica Medica*, 2019; 62: 47-52.

II Ranta I, Teuho J, Linden J, Klén R, Teräs M, Kapanen M, Keyriläinen J. Assessment of MRI-Based Attenuation Correction for MRI-Only Radiotherapy Treatment Planning of the Brain. IEEE *Diagnostics,* 2020, 20: 299.

III Ranta I, Wright P, Suilamo S, Kemppainen R, Schubert G, Kapanen M, Keyriläinen J. Clinical Feasibility of a Commercially Available MRI-only Method for Radiotherapy Treatment Planning of The Brain. *Journal of Applied Clinical Medical Physics*, 2022, [In Review].

The original publications are reproduced with the permission of the copyright holders.

Abbreviations

2D	Two-dimensional
3D	Three-dimensional
AC	Attenuation correction
AI	Artificial intelligence
AP	Anterior-posterior
BW	Bandwidth
CBCT	Cone-beam computed tomography
CC	Cranio-caudal
CT	Computed tomography
DL	Deep learning
DSC	Dice similarity coefficient
DTA	Distance to agreement
DVH	Dose-volume histogram
DWI	Diffusion-weighted imaging
EBRT	External beam radiotherapy
ED	Electron density
ELPS	External laser positioning system
EPI	Echo-planar imaging
fMRI	Functional magnetic resonance imaging
FFE	Fast-field echo
FOV	Field of view
GRE	Gradient echo
GTV	Gross tumour volume
HU	Hounsfield unit
LR	Left-right
MAE	Mean absolute error
ME	Mean error
MR	Magnetic resonance
MRAC	Magnetic resonance imaging based attenuation correction
MRCAT	Magnetic resonance for calculating attenuation

MRI	Magnetic resonance imaging
NMR	Nuclear magnetic resonance
NT	Normal tissue
NTCP	Normal tissue complication probability
OAR	Organ at risk
PET	Positron emission tomography
PTV	Planning target volume
QA	Quality assurance
RF	Radiofrequency
RT	Radiotherapy
RTP	Radiotherapy planning
sCT	Synthetic computed tomography
SD	Standard deviation
SE	Spin echo
SPM	Statistical parametric mapping
SRT	Stereotactic radiotherapy
TCP	Tumour control probability
TE	Echo time
TR	Repetition time
TPS	Treatment planning system
Tyks	Turku University Hospital

1 Introduction

1.1 Magnetic Resonance Imaging for Radiotherapy Treatment Planning of the Brain

Magnetic resonance imaging (MRI) is a widely used imaging technique for radiotherapy treatment planning (RTP) of the brain and many other anatomical sites [1]. The physical basis of modern clinical MRI lies in quantum mechanics, more specifically in the nuclear magnetic resonance (NMR) phenomenon of hydrogen nuclei, i.e., protons. By using strong external magnetic fields and radiofrequency (RF) electromagnetic pulses, protons abundant in various tissues can be excited. When the excited protons return to their equilibrium state after the excitation pulse, the nuclei emit RF electromagnetic radiation. The emitted RF radiation can then be observed with receiver coils specifically designed for the task.

By carefully manipulating the direction and magnitude of the magnetic field with gradient magnetic fields and the waveform of the RF excitation pulses over time in a predetermined sequence, it is possible to encode the emitted RF information, i.e., the NMR signal, and record the magnetic resonance (MR) data. Using the recorded RF information and appropriate Fourier transformations, it is possible to compute the final MR images. Basically, MRI contains information about the proton density of tissues [2]. However, several imaging parameters affect the quality and contrast of the final image. These parameters are selected prior to each imaging session based on clinical objectives.

The advantages of MRI over computed tomography (CT) from the perspective of brain RTP are the excellent contrast of soft tissues and the ability to manipulate the contrast between different tissue types by selecting different imaging sequences. This enables a more precise definition and delineation of the gross tumour volumes (GTV) and the organs at risk (OAR) [1,3].

In addition to target delineation, accurate radiation dose calculation and dose optimisation are required to achieve clinically adequate radiotherapy (RT) plan quality. In order to accurately assess the attenuation of ionising radiation in tissues, information on the electron density (ED) of the tissues is required. Imaging modalities such as CT, which require the transmission of ionising radiation to produce the radiographs, hence inherently contain the tissue ED information [4].

Therefore, CT has remained the gold standard imaging modality in modern RTP workflows.

Specialised MRI techniques such as diffusion-weighted imaging (DWI) and functional magnetic resonance imaging (fMRI) enable the imaging and quantification of tissue physiology without intravenous contrast agents or radiopharmaceuticals, which are needed in CT and nuclear medicine applications [5]. The potential of DWI and fMRI techniques in brain RTP and several other anatomical sites has been extensively investigated in recent years [6]. In addition to target and OAR delineation, DWI and fMRI can be used to monitor the RT treatment response of lesions and OARs [3,5,7]. Wider clinical adaptation of these techniques could enable adaptation of RT plans between treatment fractions based on treatment response information.

In the modern brain RTP workflow, it is common to perform an MRI in addition to a CT scan for patients undergoing brain RT. MRI data is used to identify and delineate GTVs and possible OARs in the vicinity of the treatment target more precisely than from CT images alone [1,8]. Despite the clear advantages of this dual-modality CT-MRI approach, the RTP process also has disadvantages and additional uncertainties. The challenges of MRI in the RTP setting are introduced in the following sections, focusing on the head.

1.1.1   Geometric Distortions in MRI

Because MRI uses magnetic fields that vary in magnitude and in direction over time in addition to electromagnetic RF pulses to produce a weak but measurable NMR signal, the imaging process is susceptible to multiple sources of interference. Interferences in the recorded MRI data may manifest themselves as geometric distortions or other image artefacts in the final MR images. Geometric distortions can be classified into scanner-related distortions and patient-related distortions [9].

Scanner-related Geometric Distortions

The most common sources of scanner-related distortions are static magnetic field inhomogeneity, gradient magnetic field inhomogeneity [10], and eddy currents resulting from rapid changes in magnetic field strength during imaging [11]. In general, the static magnetic field is the most homogeneous near the scanner isocentre and in the central regions of the effective field of view (FOV). Therefore, the magnitude of scanner-related geometric distortion increases rapidly towards the edges of the effective FOV due to the increased inhomogeneity of the magnetic field [12,13].

Scanner-related geometric distortions caused by field inhomogeneity can be significantly reduced by passive shimming of the static magnetic field [14,15]. Modern MR image processing also utilises additional geometric distortion correction algorithms that have been shown to effectively minimise the magnitude of scanner-related geometric distortions [9,11,13,16,17]. Correction algorithms are most commonly performed as an additional image processing step.

The type of imaging sequence has a significant effect on the magnitude of geometric distortions [12,13,16,18]. More advanced imaging techniques, such as echo-planar imaging (EPI), which uses a very short echo time and rapidly changing gradients, or DWI, which requires the use of additional weak gradient fields, are more prone to geometric distortions than traditional spin echo (SE) or gradient echo (GRE) based sequences [12,13,16,18].

The magnitude of scanner-related and geometric distortion has been studied carefully in recent years as MRI scanner technology and geometric distortion measurement methods have developed, because the measurement of scanner-related geometric distortion is an essential part of the quality assurance (QA) of an MRI scanner. A common approach in geometric distortion QA has been to estimate geometric distortion over a larger area using a phantom designed to fit inside the MRI head coil. An example of this type of measurement is the geometric distortion measurement proposed by the American College of Radiology MRI Quality Control Manual [19]. However, this type of measurement does not provide an estimate of local distortions nor an estimate of geometric distortions in the entire effective FOV of the MRI scanner. Due to these limitations, designated MRI geometric distortion measurement methods and QA solutions have been developed.

Mapping and quantification of scanner-related geometric distortion has been performed in previous studies using several phantom-based methods [13,20–22]. The principle behind most of these measurement methods has been to use a phantom with a known, preferably large, array of measurement points that can be visualised on MR images. Comparing the known, physical dimensions of the used phantom with the dimensions observed on the MR images provides a direct measure of the geometric distortion at each measurement point. Interpolation between individual measurement points can then be used to obtain a more detailed geometric distortion map across the entire usable FOV. Currently, several commercial solutions use fiducial marker array phantoms to measure scanner-related geometric distortion.

Patient-related Geometric Distortions

Patient-related geometric distortions are a more diverse topic than scanner-related effects. Physically, patient-related distortions are caused by differences in magnetic susceptibility between tissues, defined by the chemical structure of the tissue [23]. Therefore, differences in susceptibility affect the resonance frequency of the proton nuclei found in the tissue [24]. Magnetic field differences within a tissue or image voxel are called chemical shift [25]. They cause resonance frequency and phase differences to accumulate between the proton nuclei, creating geometric distortion and areas of signal loss on MR images [17,26]. Geometric distortions due to susceptibility differences are most significant at tissue interfaces with large susceptibility differences, e.g., air cavities, metallic implants, and dental fillings. Rapid changes in the magnetic field also cause eddy currents that weaken the MRI signal [27,28].

Reduction of patient-related geometric distortions can be accomplished by using active shimming techniques on both static and gradient magnetic fields [11,29]. At the scanner hardware level, active shimming is possible by adding dedicated shimming coils capable of producing weak magnetic fields. The shim coils can be adjusted individually before scanning to account for the magnetic field inhomogeneity caused by patients and scanning equipment.

Distortions caused by a chemical shift can routinely be observed at the interfaces of watery tissue and adipose tissue, a phenomenon commonly called fat-water shift. The magnitude of the fat-water shift in terms of image pixels can be adjusted on MRI scanners by changing the bandwidth (BW) of the RF receiver. Essentially, widening the receiver BW allows each image voxel to contain a wider frequency range of RF signal data, reducing the fat-water shift. Conversely, wider BW tends to increase noise in MR images, which may lead to clinically insufficient image quality [30].

1.1.2   Co-registration Uncertainties

The traditional way to utilise additional information from MR images is co-registration of the MR images with the CT images, thereby obtaining the attenuation information needed for dose calculation and further optimisation. In a clinical setting, this co-registration is typically performed using rigid alignment of these two sets of images. Although patient fixation methods and the use of automatic co-registration algorithms reduce the systematic error introduced by this process, the co-registration uncertainties of 1.8 mm have been reported in the head when using automatic co-registration methods [31].

Co-registration uncertainties affect the delineation process and increase the margin requirement between the GTVs and planning treatment volumes (PTV), thus increasing the irradiated tissue volume. These factors may decrease the tumour

control probability (TCP) and increase the normal tissue complication probability (NTCP). In the brain, this effect is pronounced in stereotactic radiotherapy (SRT), where the GTVs are smaller, i.e., less than 5 cm in diameter. SRT planning typically requires smaller margins of up to 1 mm to reduce the acute and chronic toxicity of RT due to the use of larger fraction sizes [32].

In modern image-guided brain RT workflows, another source of co-registration uncertainty is introduced during patient positioning imaging. During the patient positioning, radiographs using kilovoltage (kV) x-ray images are acquired and co-registered with the RTP images. Therefore, any co-registration uncertainties that arise during the RTP process are emphasised during patient positioning. The magnitude of co-registration uncertainty also affects the required PTV margin. If the uncertainties of co-registration can be reduced, it is also possible to reduce the PTV margin and possibly increase the TCP [33].

1.2 MRI-only Radiotherapy Treatment Planning of the Brain

To maximise the benefits of using MRI for GTV and OAR delineations while reducing uncertainties from CT-MRI co-registration, the use of MRI as the sole imaging modality for brain RTP has been extensively studied over the past 20 years. Due to the lack of explicit ED information on MR images, the first step in the development of MRI-only methods is the evaluation of radiation attenuation by generating synthetic computed tomography (sCT) images based on MRI data.

In previous studies, numerous methods have been used to generate brain sCT images. The prerequisite for all sCT image generation approaches is the segmentation of MRI image into different tissue types, and their assignment into Hounsfield unit (HU) values [34].

1.2.1 Brain MR Image Segmentation for sCT Image Generation

The earliest segmentation methods for brain MR images are based on manual contouring and classification of tissues by experienced radiologists or other qualified professionals trained for this task. The image segmentation process with this manual approach is both laborious segmentation quality is strongly dependent on experience and other human factors [35]. This significantly limits the usefulness of manually segmented sCT image generation in routine clinical workflows [36].

The first semi-automatic and automatic methods for segmentation of brain MR images relied on traditional image processing methods, i.e., thresholding, statistical models, and clustering [37], to accelerate the image segmentation process. However,

variations in image quality or anatomical abnormalities, which are particularly common in patients with brain tumours, pose significant challenges to simplified segmentation methods. Therefore, additional input may be often required from the user to assess the segmentation quality and perform corrections to the segmented image.

Atlas-based automatic segmentation models were developed to improve the overall segmentation quality and reduce the variation between cases. Atlas-based autosegmentation methods use prior knowledge from previously gathered anatomical MRI data collected specifically to generate a segmentation database, i.e., the atlas. Essentially, high-quality anatomical MRI data included in the atlas have been manually segmented to provide a gold standard reference against which subsequent MRI data are compared [38]. Ultimately, the quality of the anatomical atlas and its appropriateness to the segmentation task will affect the performance of the atlas-based model.

Compared with simpler segmentation methods that do not utilise prior knowledge, the atlas-based autosegmentation methods require co-registration of the MR images to be segmented with the atlas. The information from the co-registered MR images is then compared with the atlas to produce segmented MR images [39]. Several different approaches have been studied successfully in the past for atlas-based brain image autosegmentation [38].

The segmentation quality of atlas-based models can be further improved by including several atlases in the segmentation algorithm [40–42]. In the brain, the use of these multi-atlas methods is useful in cases of anatomical abnormalities, as the subsequent atlases can be included to account for e.g. resection cavities or trepanations which are common in surgical brain RT candidates.

The advent of artificial intelligence (AI) based image processing techniques such as machine learning and deep learning (DL) has enabled the development of image segmentation methods that do not require atlas data to produce segmented MR images. However, training data comparable to an anatomical atlas are required when designing and training an AI-based algorithm for an MRI segmentation task [43]. In the brain, DL-based segmentation methods have attracted the most research interest in recent years [44–47]. The primary advantages of DL-based segmentation methods are the short segmentation time after the training phase of the method and the possibility to include information from multiple sequences to generate images.

1.2.2   sCT Generation Methods

The earliest sCT generation methods studied in the context of brain RTP were based on the simplified assumption that the ED value of water would resemble the ED values of brain tissue and produce clinically acceptable RT plans with sufficient

dosimetric accuracy when treating small-volume metastases [48]. This single density approach can produce a dose calculation accuracy of less than 2% from sCT plans compared with reference CT plans [49,50].

To iterate this approach, ED values for bone tissue could also be represented by a single bulk value, which was shown to increase the dosimetric accuracy to less than 1% compared with CT-based RT plans [50]. These bulk density based sCT generation methods have since been refined to include additional ED values, such as air, compact bone, and spongy bone, white matter, and grey matter. The prerequisite for adding other tissue types is that they can be segmented from the source MR images. Adding several tissue classes has been shown to further improve the accuracy of dose calculation, with several studies reporting differences of less than 0.5% compared with CT-based RT plans [51].

More recently, sCT generation methods with continuous HU values have been developed to account for tissue inhomogeneity and further improve the quality of sCT images. The sCT generation methods with continuous HU values have been shown to significantly improve mean absolute error (MAE) results compared with bulk density methods [52,53]. The continuous HU value assignment method offers limited improvements in dosimetric accuracy compared with bulk density HU methods [34], but the use of continuous HU values significantly improves the overall image quality of sCT images to a more CT-like appearance, which is useful for confirming patient positioning.

The Analogy Between sCT Generation and MRI-based Attenuation Correction

The process for generating sCT images from MRI data is essentially analogous to generation of a magnetic resonance imaging based attenuation correction (MRAC) map developed for the needs of hybrid positron emission tomography (PET)-MRI [54]. Due to this analogy, there has been some research interest in the application of MRAC-based sCT generation methods in the RT environment. Potential advantages of the MRAC-based sCT generation methods for both PET-MRI and RT would be the ability to perform a diagnostic PET examination and MRI-only RTP imaging in the same imaging session. The additional diagnostic value provided by PET images could then be applied directly to the delineation of RT targets [55]. Although the number of studies regarding the feasibility of the MRAC-based sCT generation method is currently limited, a dose calculation difference of less than 1% compared to CT-based RT plans has been reported in the brain [56,57].

1.2.3 Considerations for the Evaluation of Plan Quality and Patient Positioning Accuracy

Accuracy of planning image geometry and dose calculation are important measures of plan quality. Although the selected sCT generation method has a large impact on the quality of the RT plan, there are several other factors that influence the assessment of dosimetric and patient positioning accuracy, which may complicate the clinical feasibility assessment of MRI-only planning compared with CT-based RTP.

The choice of MRI sequence used in RTP imaging has a significant impact on image contrast and geometric accuracy of the sequence, both of which affect the ability of sCT algorithms to segment and produce an accurate representation of the original anatomy with correctly assigned HU values relative to the CT image [34,58].

Secondly, the quality of the sCT-based plan depends in part on the configuration of the treatment planning system (TPS), as several technical factors affect the final dose calculation result. The selected ED calibration curve for HU values has a global effect on both CT and sCT images. If the calibration curves differ between the two sets of images, the results of the dose calculation will vary slightly between the sets of images [59,60]. The size of the dose calculation grid used also affects the results of the dose calculation [61], particularly if the treatment targets are small or steep dose gradients are required. Therefore, the dose calculation grid size should be equal between CT- and sCT-based RT plans when performing dosimetric evaluations.

2 Aim of the Thesis

The aim of this work was to evaluate the clinical feasibility of MRI-only based RTP of the brain and to advance the possibilities of a clinical MRI-only workflow for patients receiving external beam radiotherapy (EBRT) of the brain at Turku University Hospital (Tyks, Turku, Finland). This main aim was divided into the specific aims presented in detail in the original publications (I-III):

I.   To investigate the geometric accuracy of MRI-only RTP of the brain using modern MRI scanners and to evaluate the performance of a current clinical QA method to verify geometric accuracy.

II.   To investigate the accuracy of dose calculation of sCT images generated using the MRAC-based method for MRI-only RTP of the brain.

III. To evaluate the clinical feasibility of a commercial sCT generation algorithm for MRI-only RTP for patients with glioma and brain metastases, including assessment of dose calculation accuracy and patient positioning accuracy.

3 Materials and Methods

3.1 Imaging

3.1.1 MRI

The MRI in this work was performed with a 1.5 T Philips Ingenia (Philips Medical Systems International B.V., Best, Eindhoven, The Netherlands) MRI unit located at the Department of Oncology and Radiotherapy of Turku University Hospital (Tyks, Turku, Finland). In Study I, two additional 1.5 T and three additional 3.0 T Philips Ingenia MRI scanners located at the Tyks diagnostic imaging units and the Philips facility (Philips Oy, Vantaa, Finland) were used to collect data on scanner-dependent variation of geometric distortion.

The 1.5 T scanner located at the RT department is shown in Figure 1. The MRI device is primarily used for RTP imaging and is and is equipped with an external laser positioning system (ELPS) (LAP DORADOnova MR3T, LAP GmbH Laser Applikationen, Lüneburg, Germany). ELPS is used to visualise the origin of the image on the skin surface, allowing physical markings to be made on the patients' skin or fixation devices. The scanner can be equipped with a flat patient couch top, which enables the use of patient fixation devices and enables RTP imaging in the treatment position.

Figure 1. Philips Ingenia 1.5 T MR-RT magnetic resonance imaging (MRI) system and the LAP DORADOnova MR3T external laser positioning system (ELPS) located at the Department of Oncology and Radiotherapy of Turku University Hospital (Tyks, Turku, Finland).

In Study I, Philips geometric QA imaging protocols with GRE-based sequences were used to acquire MRI data.

In Study II, 3D mDixon MR images were acquired after gadolinium contrast agent injection in 10 glioma and 10 brain metastasis patients during standard RTP MRI sessions.

In Study III, 3D mDixon based imaging sequence included in the commercial MRCAT (magnetic resonance for calculating attenuation) Brain software (version 4.0, Philips Oy, Vantaa, Finland) for sCT generation in the brain was used to acquire MRI image data for all patients.

The relevant imaging parameters for Study I are presented in Table 1 and for Studies II and III in Table 2. The Philips 3D geometric distortion correction algorithm was used in all studies.

Table 1. Relevant magnetic resonance imaging (MRI) parameters used in the geometric distortion quality assurance (QA) scans performed in Study I (TE: echo time, TR: repetition time, BW: bandwidth, 3D: three-dimensional, 2D: two-dimensional).

Sequence	Name	TE [ms]	TR [ms]	Flip angle [°]	Acq. Matrix [px]	Voxel size [mm]	Slice thickness, gap [mm]	Image stacks, slices	BW [Hz]
T$_1$-w 3D GRE	3D geometric fidelity QA	3.4	6.7	15	512	1.09×1.09×1.00	2, -1	1, 400	431 (862)
T$_1$-w 3D GRE	2D geometric fidelity QA	3.4	6.7	15	512	1.09×1.09×1.00	2, -1	7, 25	217

Table 2. Relevant magnetic resonance imaging (MRI) parameters used in the patient scans in Studies II and III (TE: echo time, TR: repetition time, BW: bandwidth, 3D: three-dimensional, FFE: fast-field echo).

Sequence	Acq. matrix [mm³]	Recon. matrix [mm³]	TE1/TE2 [ms]	TR [ms]	Flip angle [°]	BW [Hz]	Scan time [min:s]
T1 3D FFE mDIXON (Study II)	1.1×1.1×1.4	0.68×0.68×1.0	2.0/4.4	6.8	20	481.5	5:38
T1 3D FFE mDIXON (Study III)	1.1x1.1x1.4	0.68x0.68x1.0	2.0/4.4	6.8	20	481.0	2:56

3.1.2   CT and CBCT

CT imaging for Studies II and III was performed using a Toshiba Aquilion LB (Toshiba Corp., Tokyo, Japan) CT scanner located at the Tyks RT department. Head CT imaging for Studies II and III was performed using similar imaging parameters with 120 kV tube voltage and 50 mA tube current. CT images were reconstructed using a filtered back projection algorithm with a reconstruction resolution of 1.0×1.0 cm^2. The thickness of the reconstruction slice was 2.0 mm and 1.0 mm for glioma patients and brain metastasis patients, respectively.

Cone-beam computed tomography (CBCT) in Study III was performed during clinical RT treatment sessions with Varian TrueBeam linear accelerators (Varian Medical Systems Inc., Palo Alto, CA, USA) at the Tyks RT department. The systems were equipped with kV on-board imaging systems that enable image-guided radiotherapy. CBCT images were acquired using a clinical head CBCT

protocol at 100 kV tube voltage, 10 mA tube current, 0.5×0.5 cm^2 reconstruction matrix, and 2 mm reconstructed slice thickness for both the above-mentioned patient subgroups.

3.2   Phantoms

In Study I, two QA phantoms designed for measurement of scanner-induced geometric distortion were used. The phantoms are shown in Figure 2. A prototype three-dimensional (3D) geometric QA phantom (Philips Medical systems International B.V., Best, Eindhoven, The Netherlands) was used to assess longitudinal and scanner-dependent geometric distortions. The geometric 3D QA phantom contained a structure of seven acrylic sheets with a set of 1932 embedded oil marker capsules from which the geometric distortion could be calculated. The 3D phantom covered a cylindrical volume with a diameter of 500 mm and a length of 330 mm.

A two-dimensional (2D) geometric QA phantom (Philips Medical Systems International B.V., Best, Eindhoven, The Netherlands) was a simplified version of the prototype 3D QA phantom and intended for routine geometric distortion QA. The geometric 2D QA phantom was a single acrylic sheet with a set of embedded oil marker capsules and an acrylic base for phantom alignment. The effective measurement area of the phantom was 450×550 mm^2.
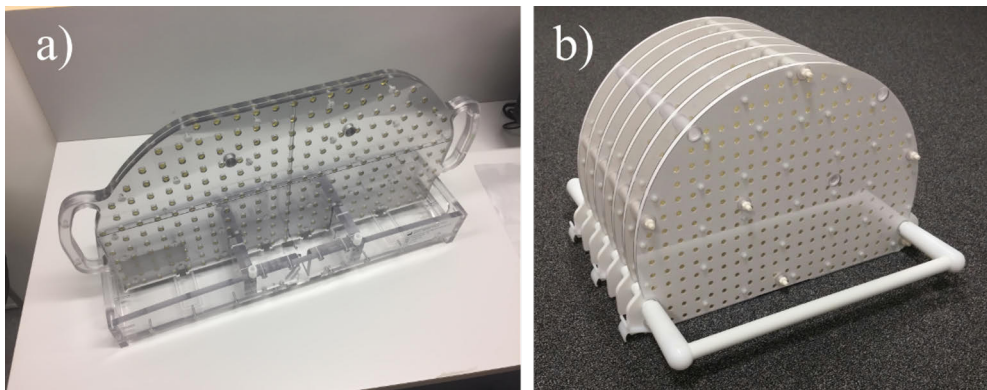

Figure 2. Geometric distortion quality assurance (QA) phantoms used in Study I. a) A two-dimensional (2D) geometric QA phantom. b) A three-dimensional (3D) geometric QA phantom.

3.3 Patient Cohorts

In Study II, 20 cancer patients who received EBRT with 6 MV photon beams at the Tyks RT department were retrospectively selected. Based on patient diagnosis, the patient cohort was divided into subgroups of glioma and brain metastasis patients, with 10 patients in each subgroup.

In Study III, 25 glioma patients and 25 brain metastasis patients were retrospectively selected for the assessment of dosimetric accuracy. Additionally, 10 glioma patients and 10 brain metastasis patients were retrospectively selected for the assessment of patient positioning accuracy.

The Studies II and III were approved by the Ethical Committee of the Hospital District of Southwest Finland (reference code: Dnro 116/1801/2017, approval date: November 21st, 2017, renewal date: November 2nd, 2020).

3.4 Measurement of Geometric Distortion

In Study I, 2D geometric QA phantom MR images were automatically analysed with Philips proprietary analysis software included in the MR-RT package as part of routine QA testing. The analysis program produced distortion maps with 1 mm, 2 mm, 3 mm, and 5 mm isocontour lines for graphical evaluation of scanner 2D geometric distortion at 0 mm ±60 mm, ±130 mm, and ±200 mm distances from the scanner isocentre. These image sets were qualitatively compared with the 3D geometric QA scan results acquired with the same scanner to assess the clinical feasibility of the 2D geometric QA method as part of routine QA.

3D geometric QA data were analysed using the Philips command-prompt based analysis software that was specifically developed to identify the locations of 3D QA phantom markers based on an intensity-weighted centre of gravity determined from MRI data. The marker locations were then compared with the reference marker locations defined in the software files to calculate the 3D geometric distortions at each marker location [62]. To account for phantom positioning uncertainty, the software also detected a global offset value in each coordinate direction. The software automatically rejected marker locations that could not be reliably identified due to low image intensity or aliasing. In these locations, the magnitude of the geometric distortions could have been more than 12 mm.

The 3D geometric QA distortion data were further processed by defining four clinically relevant ranges of interest from the scanner isocentre: 100–150 mm, 150–200 mm, 200–250 mm, and 250–290 mm. Mean distortion values for each of the four ranges were determined and scatterplots were generated from the individual distortion data points.

3.5 Generation of the sCT Images

In Study II, sCT images were generated using the previously developed MRAC method [63]. It used the atlas-based, open source SPM12 (The Wellcome Centre for Human Neuroimaging, UCL, Queen Square Institute of Neurology, London, The United Kingdom) segmentation utility to segment six different tissue classes from acquired patient MRI data, including cortical bone, spongy bone, air, grey matter, white matter, and cerebrospinal fluid. After segmentation, the tissue classes were assigned to discrete HU values based on the literature to generate sCT images. Finally, the sCT images were co-registered and resampled to match the resolution of the reference CT images.

In Study III, sCT images were generated using the commercial MRCAT Brain algorithm. It is a DL-based image segmentation method to convert mDixon MRI data into sCT images, with a continuous HU value conversion curve instead of a tissue-specific bulk HU value assignment.

3.6 Evaluation of Bone Segmentation in sCT Images

The segmentation performance of the sCT generation algorithm used in Study II was investigated using several metrics. The success of skull bone segmentation was evaluated by calculating and comparing bone volumes in both CT and sCT images. In addition, the Dice similarity coefficients (DSC) for the co-registered skull bone volumes were determined according to formula [64]:

$$DSC = \frac{2|A \cap B|}{|A| + |B|} \quad , \quad (1)$$

where A and B are segmented bone volumes. With DSC it is possible to evaluate the similarity of sCT images compared with CT images.

The similarity of HU values was also evaluated by calculating the MAE of HU values in segmented bone tissues.

3.7 Dose Calculation Accuracy of sCT-based Radiotherapy Plans

In Studies II and III, the accuracy of dose calculation was evaluated by performing a relative dosimetric comparison between CT and sCT plans. The evaluation was performed retrospectively using clinical, CT-based RT plans as reference in both Studies II and III. The dosimetric evaluation was performed in the Varian Eclipse TPS (version 15.6., Varian Medical Systems Finland Oy, Helsinki, Finland). The sCT plans were first imported into TPS, and in Study III, the CT and sCT images

were co-registered according to the skull bone structures using the Eclipse rigid co-registration tool with six degrees of freedom. The co-registration step was not necessary in Study II, as the CT and sCT images were co-registered and resampled as part of the sCT generation process.

In both Studies II and III, the CT-based RT plans including planning structures were duplicated over the co-registered sCT images, and the RT plans were recalculated with the identical RTP parameters to those of the CT-based plans. Assessment of dose calculation accuracy was performed by comparing several dose-volume histogram (DVH) parameters as recommended in the Report 83 of the International Commission on Radiation Units and Measurements [65]. Parametric comparisons were performed for PTV volumes and separate OAR (Study II) or normal tissue (NT, Study III) structure. OAR and NT structures were defined in both Studies II and III as the tissue volume contained within 2 cm from the edge of the PTV. Comparison of the CT- and sCT-based RT plans for each DVH parameter was performed by calculating the relative dose difference according to the following formula:

$$\Delta D(V) = \frac{D_{sCT}(V) - D_{CT}(V)}{D_{CT}(V)} \qquad , \quad (2)$$

where D is the radiation dose, V is the structure volume, and the subscripts denote the CT- and sCT-based RT plans.

Statistical evaluations were performed for the parametric dose comparison results. In Study II, statistical significance between CT- and sCT-based RT plans was performed by performing Wilcoxon signed-rank tests for each DVH parameter. Similarly, statistical significance between glioma and brain metastasis patient subgroups was evaluated with the Mann-Whitney U-test. In Study III, the difference between CT- and sCT-based RT plans was evaluated with a two-sample t-test for paired samples.

3.8   Gamma Analysis of Dose Distributions

To evaluate the similarity of dose distributions between the CT- and sCT-based RT plans, a global 3D gamma analysis [66] was performed for all patients in Studies II and III. In both studies, gamma evaluation was performed using several clinically relevant dose difference and distance-to-agreement (DTA) criteria. Both studies used a dose threshold of 10% of the maximum dose and a maximum gamma value of 2. Statistical difference between patient subgroups was evaluated using the Mann-Whitney U-test in Study II and the two-sample t-test for paired samples in Study III.

3.9 Evaluation of Patient Positioning Accuracy

In Study III, patient positioning accuracy based on the comparison of sCT and CT images was performed by co-registering clinical CBCT images with CT and sCT images according to the bony structures of the skull. The co-registrations were done with the automatic registration tool of the TPS. The difference between the resulting CBCT-CT and CBCT-sCT co-registrations could then be evaluated by subtracting the CBCT-sCT registration matrix from the reference CBCT-CT registration matrix. The significance of patient positioning accuracy between glioma and brain metastasis subgroups was assessed using the Wilcoxon signed-rank test.

4   Results

4.1   Assessment of Geometric Distortions

3D QA measurement demonstrated the stability of the magnitude of geometric distortions with a 1.5 T MR-RT scanner throughout the 19-month monitoring period. The performance of a dedicated 1.5 T MR-RT scanner was similar to the other two 1.5 T scanners. The geometric accuracy of the evaluated 3 T scanners was slightly poorer compared with the 1.5 T scanners at a distance of 100–250 mm from the scanner isocentre. Graphic images of the 3D QA results of the longitudinal monitoring and inter-scanner variability test are shown in Figure 3.
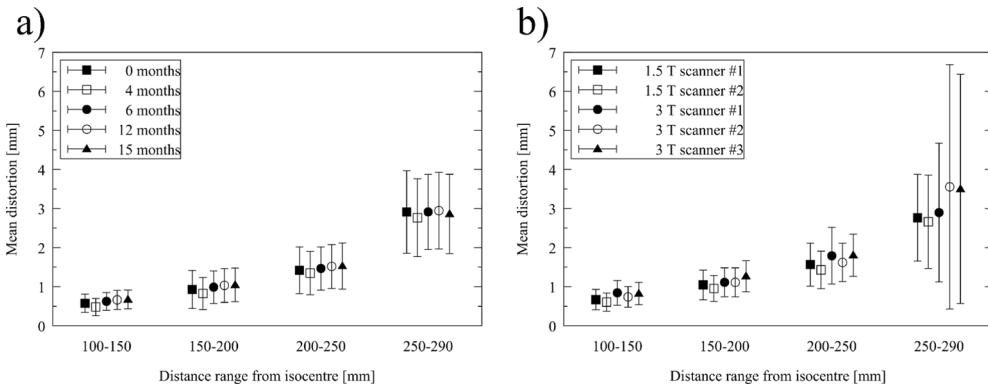
Figure 3. **a)** Evolution of the mean three-dimensional (3D) geometric distortion of the 1.5 T MR-RT platform, including the corresponding standard deviations (SD). An unintended quenching of the magnetic field occurred during the 7th month of the long-term monitoring period. **b)** 3D quality assurance (QA) results for the mean geometric distortion of all compared diagnostic scanners.

The 2D geometric QA results mirrored the 3D QA results. 2D geometric QA images showed a decrease in the effective FOV, and an increase in the magnitude of geometric distortions at greater distances from the scanner isocentre. Examples of 2D geometric QA images are shown in Figure 4.
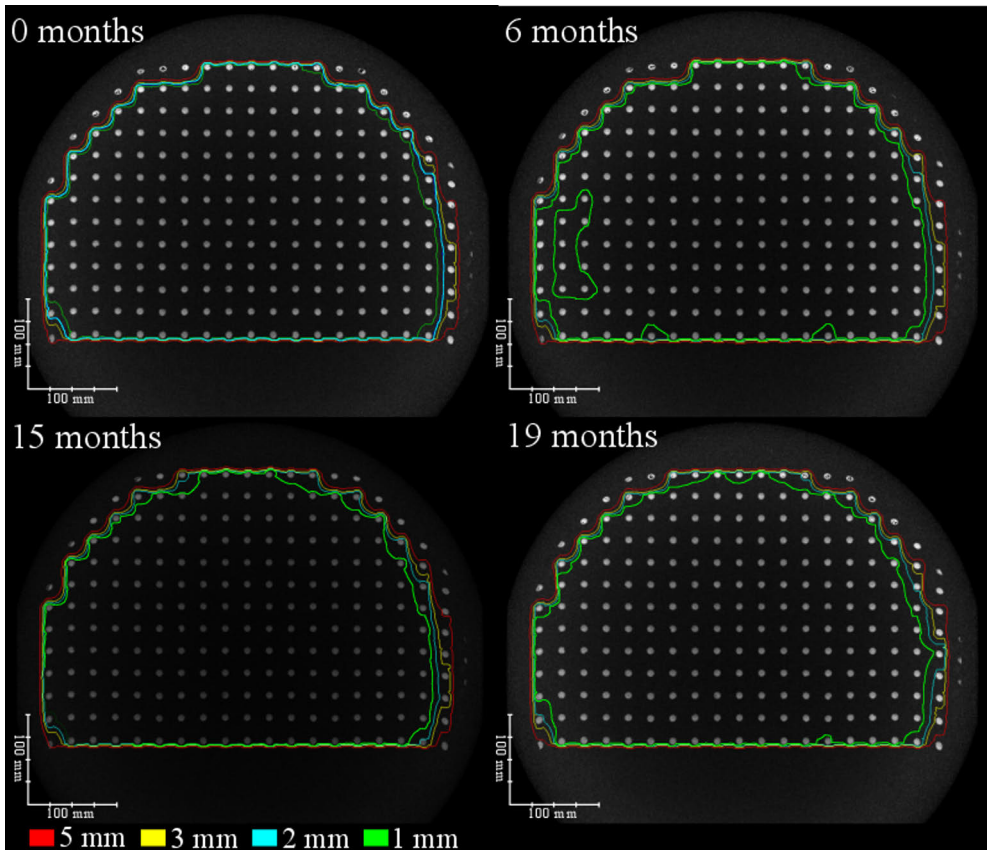
Figure 4. Examples of analysed images acquired in with the two-dimensional (2D) quality assurance (QA) test protocol during the 19-month monitoring period. The lines describe the largest geometric distortion within the defined area at a transverse distance of −130 mm from the scanner isocentre.

4.2 Evaluation of Bone Segmentation and HU Value Accuracy of sCT Images

The results of bone segmentation and HU accuracy evaluation in Study II are presented in Table 3. On average, observed bone volumes in the glioma patient subgroup were larger than in the brain metastasis patient subgroup. Statistical evaluation of relative bone volume using the Mann-Whitney U-test showed no statistical differences between the glioma and brain metastasis patient groups (p=0.13). Similarly, no statistically significant differences in DSC or MAE values were observed between the patient groups (p≥0.27).

Table 3. Bone volume (V) comparison, Dice similarity coefficient (DSC) and mean absolute error (MAE) of Hounsfield unit (HU) value results for the glioma and brain metastasis patient groups in Study II (SD: standard deviation).

Group	Glioma	Brain metastasis
Variable	Mean (SD) [Range]	
$V_{CT, bone}$ [cm^3]	220.4 (81.4) [126.6–443.1]	410.7 (59.7) [305.3–508.1]
$V_{sCT, bone}$ [cm^3]	227.4 (127.2) [128.1–585.5]	465.4 (98.1) [280.9–634.8]
ΔV_{bone} [%]	3.1 (19.5) [−34.5–32.1]	12.5 (11.8) [−8.0–26.8]
DSC_{bone} [ ]	0.8 (0.1) [0.6–0.9]	0.8 (0.0) [0.8–0.9]
MAE [HU]	142.2 (15.4) [114.4–166.7]	139.7 (11.8) [114.4–166.6]

The MAE and mean error (ME) values determined in Study III are presented in Table 4. No statistically significant differences between the glioma and brain metastasis patient groups were observed in MAE or ME values. When comparing MAE values between studies, the MAE values determined in Study III were on average significantly lower than those in Study II.

Table 4. Results for mean absolute error (MAE) and mean error (ME) of Houndsfield unit (HU) values in Study III for glioma and brain metastasis patient groups (SD: standard deviation).

Group	Glioma	Brain metastasis
Parameter	Mean (SD) [Range] [HU]	
MAE	63.6 (8.7) [50.4 – 82.1]	66.8 (8.6) [57.0 – 83.2]
ME	1.1 (8.1) [-10.5 – 17.0]	2.1 (7.5) [-10.6 – 20.0]

4.3 Dose Calculation Accuracy of sCT Images for Radiotherapy Treatment Planning of the Brain

The dose calculation results of glioma and brain metastasis patients in Study II are presented in Figure 5. The results showed that the mean relative difference between sCT-based RT plans and clinical CT-based plans was 0.2% in glioma patients and -0.4% in brain metastasis patients when comparing mean PTV doses. Mean OAR doses showed a difference of 0.1% and 0.6% in glioma patients and brain metastasis patients, respectively.
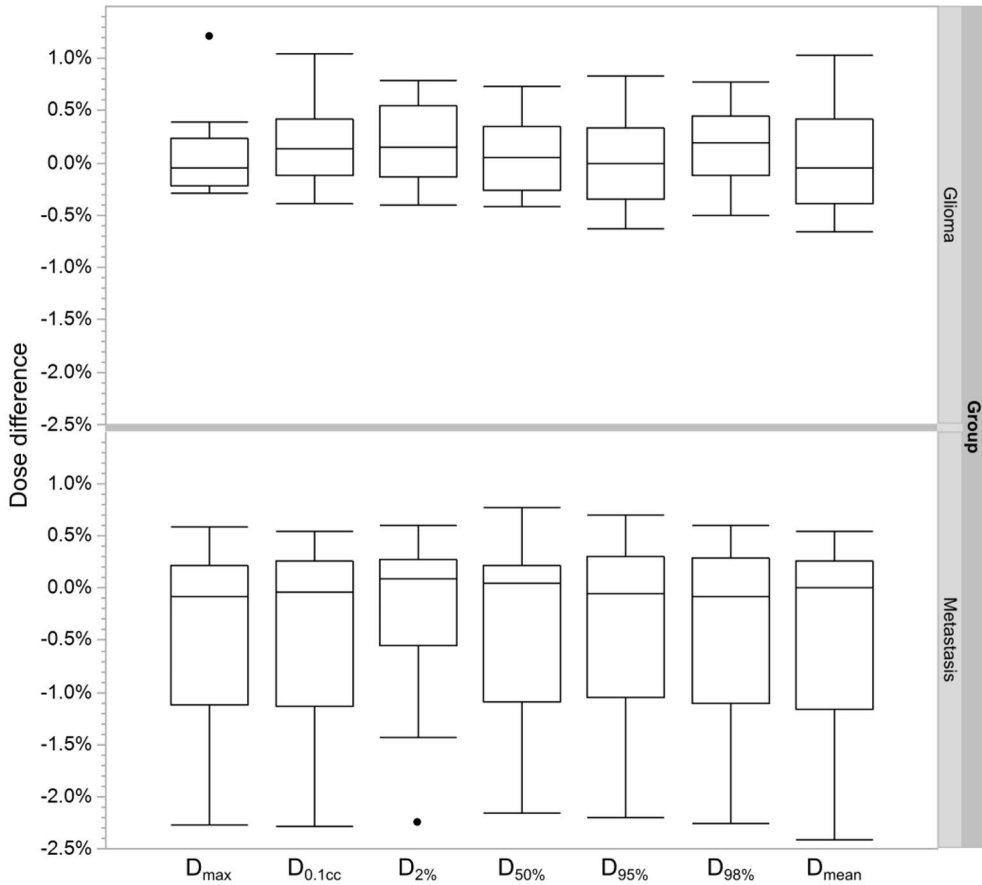
Figure 5. Dose-volume histogram (DVH) parametric comparison results for planning target volume (PTV) in glioma and brain metastasis patient groups in Study II.

Table 5 shows the results of 3D global gamma analysis results for the glioma and brain metastasis patient groups in Study II. Based on the statistical evaluation, there was a significant difference in the pass rates between the groups (p=0.04) when using the 2%/2mm criterion.

Table 5. Gamma analysis results for glioma and brain metastasis patient groups in Study II. (SD: standard deviation)

Group	Glioma	Brain metastasis
Agreement Criterion	Mean pass rate (SD) [range] [%]	
1%/1 mm	90.7 (3.6) [85.6–95.0]	96.5 (4.7) [84.3–100.0]
2%/2 mm	95.7 (0.9) [93.9–96.8]	99.9 (0.3) [99.1–100.0]

The dose calculation accuracy results of the glioma and brain metastasis patient groups in Study III are presented in Figure 6. Mean relative dose differences for all PTV dosimetric parameters were ≤0.6% (1.0%) in the entire patient cohort. A mean relative dose difference of ≤1.7% (3.6%) was determined for the NT DVH parameters. The results showed that the mean relative dose difference was ≤1.1% (3.6%) for all DVH parameters in the glioma patient group and ≤1.7% (2.3%) in the brain metastasis patient group. Statistical testing showed significant dose differences in PTV dose calculation accuracy results between patient groups (p<0.05) in all but the D_{max} DVH point (p=0.80).

The gamma analysis results presented in Table 6 showed a pass rate of 98.0% (2.1%) using the 2%/2 mm DTA criterion for glioma patients and a pass rate of 99.2% (2.0%) for brain metastasis patients. The stricter 1%/1 mm DTA criterion yielded a pass rate of 95.2% (8.5%) in brain metastasis patients. Overall, one outlier patient in the glioma subgroup and one outlier patient in the brain metastasis subgroup were found with a pass rate of <95% using the 2%/2 mm dose difference and DTA criterion. Statistical analysis showed a statistically significant difference (p<0.05) between patient groups at 1%/1 mm and 2%/2 mm dose difference and DTA criteria.
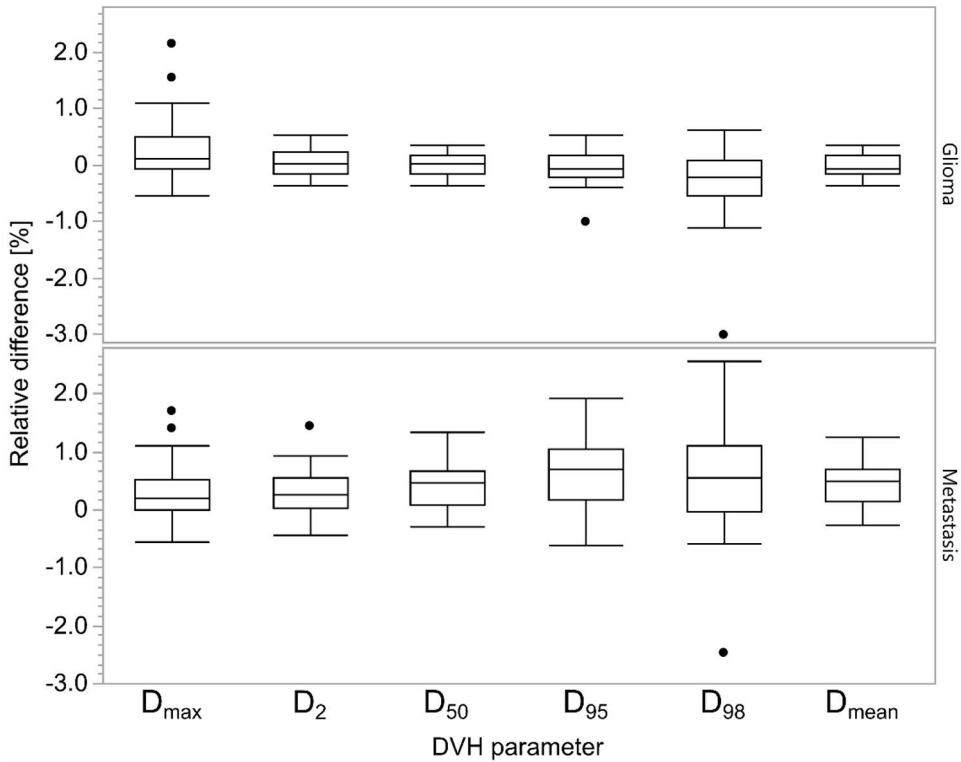
Figure 6. Dose volume histogram (DVH) parametric comparison results for planning target volume (PTV) in glioma and brain metastasis patient groups in Study III.

Table 6. Gamma analysis results for glioma and brain metastasis patient subgroups in Study III. (SD: standard deviation)

Group	Glioma	Brain metastasis
Agreement Criterion	Mean pass rate (SD) [range] [%]	
1%/1 mm	82.1 (7.6) [65.5 – 95.6]	95.2 (8.5) [68.6 – 100.0]
2%/2 mm	98.0 (2.1) [89.7 – 99.8]	99.2 (2.0) [91.0 – 100.0]
3%/3 mm	99.7 (0.5) [97.4 – 100.0]	99.8 (0.4) [98.1 – 100.0]

4.4   Patient Positioning Accuracy

In Study III, the patient positioning accuracy results presented in Figure 7 for 20 patients showed on average differences of less than 1 mm in the primary coordinate directions and ≤0.1˚ rotational differences in CBCT-based positioning between CT and sCT images in both patient groups. No statistically significant differences in positioning accuracy were observed between the groups.
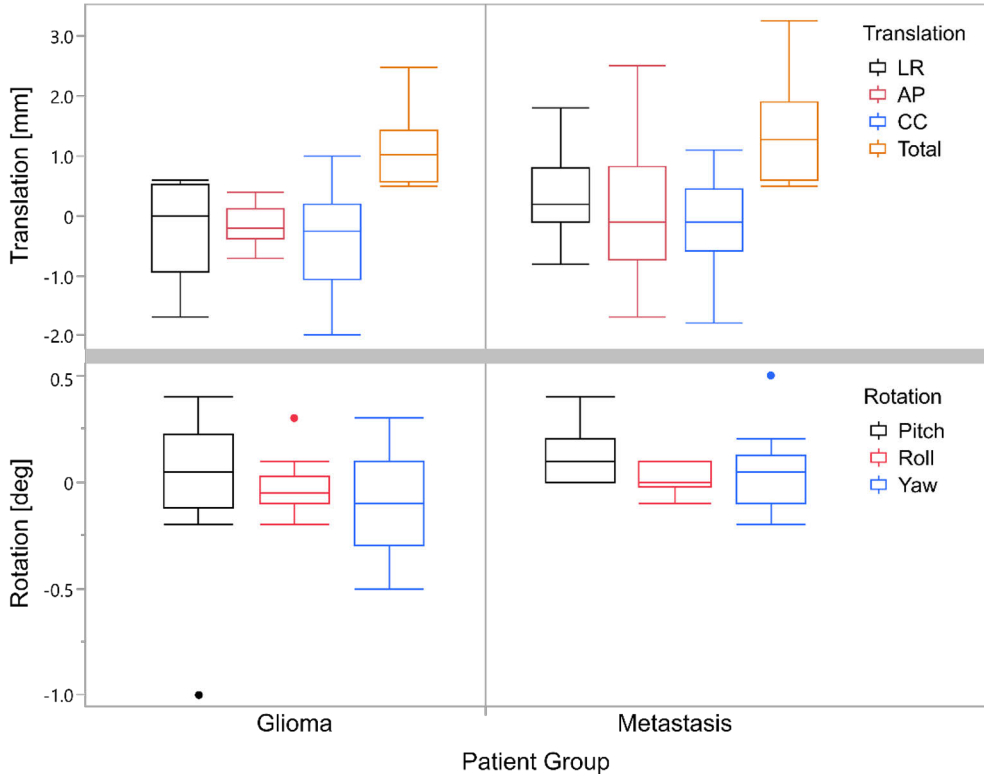
**Figure 7**. Box plots of patient positioning accuracy results of Study III for subgroups of glioma and brain metastasis patients. The total translation error is defined as the vector sum of the translation in the three primary coordinate directions (LR: left-right, AP: anterior-posterior, CC = cranio-caudal).

5   Discussion

5.1   Stability of Geometric Accuracy and the Performance of QA Methods (Study I)

In Study I, the results of QA measurements of the 3D geometric accuracy indicated that the scanner-related geometric accuracy of 1.5 T and 3.0 T MRI systems of the same generation was similar, when comparing distortions of less than 250 mm from the scanner isocentre, and independent of scanner age. This also demonstrated that the geometric accuracy performance of current MRI systems remains stable over long periods of time. In addition, no significant changes in geometric accuracy were observed during the 19-month follow-up period with a dedicated 1.5 T MR-RT scanner, despite an inadvertent shutdown of the static magnetic field during the follow-up period.

The geometric accuracy results presented in Study I were consistent with previous studies on scanner-induced geometric distortions measured using GRE-based sequences with different phantom setups and imaging settings [12,20,67–69]. Furthermore, similar geometric accuracy was reported in clinical feasibility studies of MRI-only RTP of the pelvis and brain. The results of Study I showed that the total geometric distortion was less than 1 mm at a radius of 150 mm from the scanner isocentre, and less than 2 mm at a radius of less than 200 mm from the scanner isocentre.

Determining a clinically sufficient level of geometric accuracy in the head can be done based on clinical RTP requirements. Consensus on the use of stereotactic RTP techniques suggests that the total spatial uncertainty from all possible sources should not exceed 1 mm. Therefore, geometric distortions of less than 0.5 mm should be the minimum requirement for stereotactic targets less than 20 mm in diameter. Based on the results of Study I, this condition can be met near the isocentre. This result suggests that the target region should be placed as close to the isocentre as possible.

The evaluation of the 2D QA method compared with the 3D method was clinically valuable. Based on experience, the 2D QA method was a more reproducible way to measure geometric distortions due to the structural simplicity of the 2D QA phantom and uncomplicated imaging process. Measurement results may

have some random error due to phantom alignment, but similar measurements with a large FOV 3D phantom have been shown to be insensitive to small positioning uncertainties [27].

The major limitation in evaluating of the 2D QA method compared with the 3D method was that the 2D method measured in-plane geometric distortion only semi-quantitatively, with discrete distortion values, compared to the quantitative 3D method. Even if the geometric distortions in the through-plane directions could be detected by the 2D method, the measurement sensitivity would be lower and it would lack the quantitative properties of the 3D method. Furthermore, the availability of lightweight phantoms capable of quantitative 3D measurement of geometric distortions has improved in recent years. Despite these limitations of the 2D geometric distortion QA method, the semi-quantitative measurement method is still useful in routine clinical QA if a baseline of normal scanner performance can be determined with a more comprehensive 3D measurement.

5.2 Feasibility of Dose Calculation Accuracy of MRI-only Radiotherapy Treatment Planning of the Brain Using an MRAC Method (Study II)

The results of Study II showed that dose calculation accuracy and RT plan quality with clinically feasible quality [70] can be achieved with the studied MRAC-based sCT generation method from contrast-enhanced source MR images.

Bone segmentation accuracy of sCT images was consistent with previous studies [46,71], and segmentation was able to reproduce the anatomical malformations in the skull region in patients who received post-operative RT.

The bone segmentation model was used to segment only the skull region. Therefore, further improvements of the model and bone segmentation of the oral and nasal cavities [72] could have further improved both segmentation performance and dose calculation accuracy. The results of Study II encouraged further development of the MRAC sCT generation method. Subsequent iterations of the studied method could include an extended segmentation template tailored to the head and neck region. Future studies on the performance of the iterated MRAC sCT generation method would provide valuable information on the clinical feasibility of MRI-only RTP of the head and neck region, which has been a growing area of research interest in recent years [51,70,73–75].

A limiting factor of Study II was the relatively small size of the patient subgroups, as there were 10 patients in both glioma and brain metastasis subgroups. Therefore, a more comprehensive clinical feasibility evaluation of the studied MRAC sCT generation method should be performed with a larger patient cohort in further studies.

Also, the patient positioning accuracy based on sCT images generated with the MRAC method was not investigated in Study II. In order to improve the application possibilities of the MRAC method in clinical RT use, attention should be paid to the quality of the sCTs in later versions of the MRAC method. Future validation studies could then also include quantitative evaluations of patient positioning accuracy based on the comparison of sCT and CT images.

5.3 Clinical Feasibility of MRI-only Radiotherapy Treatment Planning of the Brain (Study III)

In Study III, no clinically significant dose deviations or differences within patient subgroups were observed with the studied commercial sCT generation method. The patient positioning accuracy results demonstrated the clinical feasibility of CBCT-based positioning in both glioma and brain metastasis patient subgroups.

HU value reproducibility assessment showed mean MAE values consistent with previous studies of brain sCT generation algorithms using different approaches [45,76–79]. As a general, qualitative observation, the studied sCT generation algorithm showed a tendency to overestimate the size of air cavities. The same observation can also be made based on the MAE analysis, where the largest deviations between CT and sCT image HU values were observed near air cavities or fine bone structures. These types of issues have also been recognised in previous studies as challenges for sCT generation algorithms and are due to the absence of MR signal at tissue interfaces with large susceptibility differences [1,80].

The mean results and gamma pass rates observed in the dosimetric evaluations were similar to those obtained in previous brain studies [45,76,77,81,82]. The results of the dosimetric evaluation indicated clinically feasible pass rates [70] in both patient subgroups. Overall, there were no statistically significant differences between subgroups.

Some outlier results were observed during dose calculation accuracy evaluation and gamma analysis. Most of these were observed in patients with PTV or NT structures extending close to the skin surface or air cavities, or patients with larger than 2˚ rotational difference between CT and sCT images. Further assessments of the most severe outlier patients confirmed that large rotational differences were the main reason for the outlier results.

Previous studies of patient positioning accuracy using CBCT of the brain is rather limited, but the mean results obtained were consistent with the previous brain studies, in which CBCT was used to evaluate the clinical feasibility of another commercial MRI-only method for the brain [76,79]. Qualitatively, the image quality of the sCT images generated by the commercial sCT generation method was close

to the quality of the reference CT images, despite slight overestimations of the air cavity size and the fine bony structures of the nasopharyngeal cavity and ear canals.

Findings on the limitations of the studied MRI-only method are valuable in a clinical context, as they highlight the need for careful evaluation of dose distribution in cases where the PTV is in close proximity to air cavities or fine bone structures. Although achieving complete correspondence between CT- and sCT-based RT plans is difficult, most patients could be treated using an MRI-only workflow with the investigated, commercial sCT method. The results of Study III enable the commercial sCT generation method to be applied to routine clinical practice for patients with glioma or brain metastases.

5.4   Comparison of Commercial sCT and MRAC Methods (Study II and Study III)

The mean dosimetric accuracy and gamma agreement of the studied MRAC and commercial sCT generation methods were quite similar despite the different approaches. The overall consistency of the commercial sCT method compared better with the MRAC method, especially when comparing the metastasis subgroup results. As the PTV locations and patient cohort sizes were different in Studies II and III, a direct comparison of the results is not possible.

Compared with the mean MAE values observed for the MRAC method, the performance of the commercial sCT generation method was clearly better. The differences between the MAE results were due to two significant differences between the MRAC and sCT methods. The commercial sCT method used continuous HU value assignment compared with the bulk value HU assignment of the MRAC method. Secondly, the MRAC method included only the skull bone segmentation model, while the commercial sCT method included the segmentation of extracranial bony structures, including the spine. The lack of bone segmentation of nasal cavities in the MRAC method may have contributed to some of the dosimetric differences between the commercial sCT and MRAC methods.

The overall image quality of sCT images generated with the commercial method was significantly better compared with the sCT images generated with the MRAC method. A detailed comparison of the MRAC method and the commercial sCT method in terms of segmentation quality and dosimetric and patient positioning accuracy could be performed in future studies to provide detailed information on performance differences.

5.5   Uncertainties and Limitations

The results of Study I cannot be generalised to scanners other than those tested. In addition, since the measurement methods used were vendor-specific, MRI scanners from other manufacturers could not be tested.

In Studies II and III, the evaluations of dose calculation accuracy were performed by registering CT and sCT images and copying CT-based RT plans over sCT images. In Study III, dosimetric evaluations were performed with clinical tools. Therefore, the sCT plans were not resampled to the CT image grid, but simply registered with the CT images using six degrees of freedom. Due to the limitations of the TPS used, the rotational differences between CT and sCT images were preserved when copying CT-based RT plans, thus any remaining registration error could have been reflected in the sCT dose calculation results. This effect would be more significant in regions further from the PTV, where absolute radiation doses tend to be lower, leading to larger relative radiation dose differences. Furthermore, the results of the gamma evaluation are sensitive to registration errors due to the DTA component of the gamma agreement criteria. Re-optimisation of duplicate RT plans could have reduced the error due to co-registration differences [82]. However, investigating the possible effects of re-optimisation in dose calculation accuracy was not part of Studies II or III. Studies II and III also did not examine the potential effects of different treatment delivery setups, choice of dose calculation algorithms, or HU conversion tables on dosimetric accuracy.

As MRI-only methods have generally been adapted to routine clinical workflow only recently, the compatibility of sCT images in planning, treatment, and patient positioning may be compromised when image guidance protocols and MRI scanners from different manufacturers are used. Therefore, the generalisation of the findings of Studies II and III is only possible after further clinical validation. Since the findings of Studies II and III were based on relatively small groups of patients, the distribution of the results may differ from the results obtained from a larger group of patients.

6 Conclusions

Based on the results presented in the original publications (I–III), the following conclusions can be drawn:

I. The geometric accuracy of modern MRI scanners is adequate for MRI-only RTP scanning. The evaluated geometric accuracy methods produced important information for QA and stability monitoring in the clinical MR-RT workflow. The investigated methods are sufficient for routine geometric accuracy QA in clinical conditions, with minor improvements to the user interface and automatic calculation of distortion values.

II. The use of sCT images generated using the MRAC method may be accurate for dose calculation for MRI-only RTP of the brain. The results enable further development of the MRAC method, including bone segmentation of the nasal and oral cavities, and thus possibly extending the assessment to the head and neck region.

III. The investigated commercial sCT algorithm was shown to be a clinically feasible method for clinical MRI-only RTP for patients with glioma or brain metastases. The results encourage the judicious use of the studied method as part of the routine clinical workflow for these patients.

List of References

[1]   Schmidt MA, Payne GS. Radiotherapy planning using MRI. 2015;60(22):R323–61. https:\\doi.org\10.1088/0031-9155/60/22/R323

[2]   McRobbie DW, Moore EA, Graves MJ, Prince MR. MRI from Picture to Proton. 2017; https:\\doi.org\10.1017/9781107706958

[3]   Owrangi AM, Greer PB, Glide-Hurst CK. MRI-only treatment planning: Benefits and challenges. 2018;63(5):05TR01. https:\\doi.org\10.1088/1361-6560/aaaca4

[4]   Khan FM. The Physics of Radiation Therapy. 4th ed. Philadelphia, PA: Lippincott Williams & Wilkins; 2010.

[5]   Metcalfe P, Liney GP, Holloway L, Walker A, Barton M, Delaney GP, et al. The potential for an enhanced role for MRI in radiation-therapy treatment planning. Vol. 12, Technology in Cancer Research and Treatment. 2013. p. 429–46. https:\\doi.org\10.7785/tcrt.2012.500342

[6]   Tsien C, Cao Y, Chenevert T. Clinical Applications for Diffusion MRI in Radiotherapy. 2014;24(3):218. https:\\doi.org\10.1016/J.SEMRADONC.2014.02.004

[7]   Kovács Á, Tóth L, Glavák C, Liposits G, Hadjiev J, Antal G, et al. Integrating functional MRI information into conventional 3D radiotherapy planning of CNS tumors. Is it worth it? 2011;105(3):629–37. https:\\doi.org\10.1007/S11060-011-0633-2

[8]   Liney G, van der Heide Uulke. MRI for Radiotherapy: Planning, Delivery, and Response Assessment. :210.

[9]   Wang D, Doddrell DM. Geometric Distortion in Structural Magnetic Resonance Imaging. 2005;1:49–60.

[10]   Janke A, Zhao H, Cowin GJ, Galloway GJ, Doddrell DM. Use of spherical harmonic deconvolution methods to compensate for nonlinear gradient effects on MRI images. 2004;52(1):115–22. https:\\doi.org\10.1002/MRM.20122

[11]   Weygand J, Fuller CD, Ibbott GS, Mohamed ASR, Ding Y, Yang J, et al. Spatial precision in magnetic resonance imaging-guided radiation therapy: The role of geometric distortion. International Journal of Radiation Oncology Biology Physics. 2016. https:\\doi.org\10.1016/j.ijrobp.2016.02.059

[12]   Walker A, Liney G, Metcalfe P, Holloway L. MRI distortion: Considerations for MRI based radiotherapy treatment planning. 2014;37(1):103–13. https:\\doi.org\10.1007/s13246-014-0252-2

[13]   Torfeh T, Hammoud R, Perkins G, McGarry M, Aouadi S, Celik A, et al. Characterization of 3D geometric distortion of magnetic resonance imaging scanners commissioned for radiation therapy planning. 2016;34(5):645–53. https:\\doi.org\10.1016/j.mri.2016.01.001

[14]   Belov A, Bushuev V, Emelianov M, Eregin V, Severgin Y, Sytchevski S, et al. Passive Shimming of the Superconducting Magnet for MRI. 1995;5(2):679–81. https:\\doi.org\10.1109/77.402639

[15]   Noguchi S, Kim S, Hahn S, Iwasa Y. Passive shimming by eliminating spherical harmonics coefficients of all magnetic field components generated by correction iron pieces. 2014;50(2):605–8. https:\\doi.org\10.1109/TMAG.2013.2276736

[16] Baldwin LN, Wachowicz K, Thomas SD, Rivest R, Fallone BG. Characterization, prediction, and correction of geometric distortion in 3 T MR images. 2007; https:\\doi.org\10.1118/1.2402331

[17] Stanescu T, Jans HS, Wachowicz K, Gino Fallone B. Investigation of a 3D system distortion correction method for MR images. 2010;11(1):200–16. https:\\doi.org\10.1120/jacmp.v11i1.2961

[18] Fransson A, Andreo P, Pötter R. Aspects of MR Image Distortions in Radiotherapy Treatment Planning. 2001;177(2):59–73. https:\\doi.org\10.1007/s00066-001-0771-0

[19] American College of Radiology. Phantom Test Guidance for the ACR MRI Accreditation Program. Reston, VA: American College of Radiology,; 2005. 5 p.

[20] Walker A, Liney G, Holloway L, Dowling J, Rivest-Henault D, Metcalfe P. Continuous table acquisition MRI for radiotherapy treatment planning: Distortion assessment with a new extended 3D volumetric phantom. 2015;42(4):1982–91. https:\\doi.org\10.1118/1.4915920

[21] Wyatt J, Hedley S, Johnstone E, Speight R, Kelly C, Henry A, et al. Evaluating the repeatability and set-up sensitivity of a large field of view distortion phantom and software for magnetic resonance-only radiotherapy. 2018;6:31–8. https:\\doi.org\10.1016/J.PHRO.2018.04.005

[22] Wyatt JJ, McCallum HM, Maxwell RJ. Developing quality assurance tests for simultaneous Positron Emission Tomography – Magnetic Resonance imaging for radiotherapy planning. 2022;22:28–35. https:\\doi.org\10.1016/J.PHRO.2022.03.003

[23] Schenck JF. The role of magnetic susceptibility in magnetic resonance imaging: MRI magnetic compatibility of the first and second kinds. 1996;23(6):815–50. https:\\doi.org\10.1118/1.597854

[24] Duyn JH, Schenck J. Contributions to magnetic susceptibility of brain tissue. 2017;30(4):e3546. https:\\doi.org\10.1002/NBM.3546

[25] Hood MN, Ho VB, Smirniotopoulos JG, Szumowski J. Chemical shift: The artifact and clinical tool revisited. 1999;19(2):357–71. https:\\doi.org\10.1148/RADIOGRAPHICS.19.2.G99MR07357

[26] Stanescu T, Wachowicz K, Jaffray DA. Characterization of tissue magnetic susceptibility-induced distortions for MRIgRT. 2012;39(12):7185–93. https:\\doi.org\10.1118/1.4764481

[27] Lüdeke KM, Röschmann P, Tischler R. Susceptibility artefacts in NMR imaging. 1985;3(4):329–43. https:\\doi.org\10.1016/0730-725X(85)90397-2

[28] Lee MJ, Kim S, Lee SA, Song HT, Huh YM, Kim DH, et al. Overcoming artifacts from metallic orthopedic implants at high-field-strength MR imaging and multidetector CT. 2007;27(3):791–803. https:\\doi.org\10.1148/RG.273065087/ASSET/IMAGES/LARGE/G07MA03G15B.JPEG

[29] Sengupta S, Welch EB, Zhao Y, Foxall D, Starewicz P, Anderson AW, et al. Dynamic B0 shimming at 7 T. 2011;29(4):483–96. https:\\doi.org\10.1016/j.mri.2011.01.002

[30] Stadler A, Schima W, Ba-Ssalamah A, Kettenbach J, Eisenhuber E. Artifacts in body MR imaging: Their appearance and how to eliminate them. Vol. 17, European Radiology. 2007. p. 1242–55. https:\\doi.org\10.1007/s00330-006-0470-4

[31] Ulin K, Urie MM, Cherlow JM. Results of a multi-institutional benchmark test for cranial CT/MR image registration. 2010;77(5):1584–9. https:\\doi.org\10.1016/j.ijrobp.2009.10.017

[32] Hall EJ, Giaccia AJ. Radiobiology for the radiologist. 7th Edition. Wolters Kluwer Health; 2011. 546 p.

[33] Burnet NG, Thomas SJ, Burton KE, Jefferies SJ. Defining the tumour and target volumes for radiotherapy. 2004;4(2):153. https:\\doi.org\10.1102/1470-7330.2004.0054

[34] Edmund JM, Nyholm T. A review of substitute CT generation for MRI-only radiation therapy. 2017;12(1):28. https:\\doi.org\10.1186/s13014-016-0747-y

[35] Cardenas CE, Yang J, Anderson BM, Court LE, Brock KB. Advances in Auto-Segmentation. 2019;29(3):185–97. https:\\doi.org\10.1016/j.semradonc.2019.02.001

[36] Sharp G, Fritscher KD, Pekar V, Peroni M, Shusharina N, Veeraraghavan H, et al. Vision 20/20: Perspectives on automated image segmentation for radiotherapy. 2014;41(5):050902. https:\\doi.org\10.1118/1.4871620

[37] Balafar MA, Ramli AR, Saripan MI, Mashohor S. Review of brain MRI image segmentation methods. Vol. 33, Artificial Intelligence Review. 2010. p. 261–74. https:\\doi.org\10.1007/s10462-010-9155-0

[38] Cabezas M, Oliver A, Lladó X, Freixenet J, Bach Cuadra M. A review of atlas-based segmentation for magnetic resonance brain images. 2011;104(3). https:\\doi.org\10.1016/j.cmpb.2011.07.015

[39] D'Haese PF, Duay V, Merchant TE, Macq B, Dawant BM. Atlas-based segmentation of the brain for 3-dimensional treatment planning in children with infratentorial ependymoma. 2003;2879(PART 2):627–34. https:\\doi.org\10.1007/978-3-540-39903-2_77

[40] Aljabar P, Heckemann RA, Hammers A, Hajnal j v., Rueckert D. Multi-atlas based segmentation of brain images: Atlas selection and its effect on accuracy. 2009;46(3):726–38. https:\\doi.org\10.1016/J.NEUROIMAGE.2009.02.018

[41] Burgos N, Cardoso MJ, Thielemans K, Modat M, Pedemonte S, Dickson J, et al. Attenuation correction synthesis for hybrid PET-MR scanners: Application to brain studies. 2014;33(12):2332–41. https:\\doi.org\10.1109/TMI.2014.2340135

[42] Lee J, Carass A, Jog A, Zhao C, Prince JL. Multi-atlas-based CT synthesis from conventional MRI with patch-based refinement for MRI-based radiotherapy planning. 2017;10133:101331I. https:\\doi.org\10.1117/12.2254571

[43] Alzubaidi L, Zhang J, Humaidi AJ, Al-Dujaili A, Duan Y, Al-Shamma O, et al. Review of deep learning: concepts, CNN architectures, challenges, applications, future directions. 2021;8(1):1–74. https:\\doi.org\10.1186/S40537-021-00444-8

[44] Han X. MR-based synthetic CT generation using a deep convolutional neural network method. 2017;44(4):1408–19. https:\\doi.org\10.1002/MP.12155

[45] Dinkla AM, Wolterink JM, Maspero M, Savenije MHF, Verhoeff JJC, Seravalli E, et al. MR-Only Brain Radiation Therapy: Dosimetric Evaluation of Synthetic CTs Generated by a Dilated Convolutional Neural Network. 2018;102(4):801–12. https:\\doi.org\10.1016/j.ijrobp.2018.05.058

[46] Kazemifar S, Mcguire S, Timmerman R, Wardak Z, Nguyen D, Park Y, et al. MRI-only brain radiotherapy: Assessing the dosimetric accuracy of synthetic CT images generated using a deep learning approach. 2019;136:56–63. https:\\doi.org\10.1016/j.radonc.2019.03.026

[47] Maspero M, Bentvelzen LG, Savenije MHF, Guerreiro F, Seravalli E, Janssens GO, et al. Deep learning-based synthetic CT generation for paediatric brain MR-only photon and proton radiotherapy. 2020;153:197–204. https:\\doi.org\10.1016/j.radonc.2020.09.029

[48] Schad LR, Blüml S, Hawighorst H, Wenz F, Lorenz WJ. Radiosurgical treatment planning of brain metastases based on a fast, three-dimensional MR imaging technique. 1994;12(5):811–9. https:\\doi.org\10.1016/0730-725X(94)92206-3

[49] Prabhakar R, Julka PK, Ganesh T, Munshi A, Joshi RC, Rath GK. Feasibility of using MRI alone for 3D radiation treatment planning in brain tumors. 2007;37(6):405–11. https:\\doi.org\10.1093/jjco/hym050

[50] Kristensen BH, Laursen FJ, Løgager V, Geertsen PF, Krarup-Hansen A. Dosimetric and geometric evaluation of an open low-field magnetic resonance simulator for radiotherapy treatment planning of brain tumours. 2008;87(1):100–9. https:\\doi.org\10.1016/j.radonc.2008.01.014

[51] Jonsson JH, Karlsson MMG, Karlsson MMG, Nyholm T. Treatment planning using MRI data: an analysis of the dose calculation accuracy for different treatment regions. 2010;5(1):62. https:\\doi.org\10.1186/1748-717X-5-62

[52] Yu VY, Keyrilainen J, Suilamo | Sami, Ilyes Beslimane |, Dresner A, Halkola | Aleksi, et al. A multi-institutional analysis of a general pelvis continuous Hounsfield unit synthetic CT software for radiotherapy. 2021;22(3):207–15. https:\\doi.org\10.1002/acm2.13205

[53] Spadea MF, Maspero M, Zaffino P, Seco J. Deep learning based synthetic-CT generation in radiotherapy and PET: A review. 2021;48(11):6537–66. https:\\doi.org\10.1002/mp.15150

[54] Chen Y, An H. Attenuation Correction of PET/MR Imaging. 2017;25(2):245. https:\\doi.org\10.1016/J.MRIC.2016.12.001

[55] Johansson A, Garpebring A, Karlsson M, Asklund T, Nyholm T. Improved quality of computed tomography substitute derived from magnetic resonance (MR) data by incorporation of spatial information--potential application for MR-only radiotherapy and attenuation correction in positron emission tomography. 2013;52(7):1369–73. https:\\doi.org\10.3109/0284186X.2013.819119

[56] Wiesinger F, Sacolick LI, Menini A, Kaushik SS, Ahn S, Veit-Haibach P, et al. Zero TE MR bone imaging in the head. 2016;75(1):107–14. https:\\doi.org\10.1002/mrm.25545

[57] Arabi H, Koutsouvelis N, Rouzaud M, Miralbell R, Zaidi H. Atlas-guided generation of pseudo-CT images for MRI-only and hybrid PET-MRI-guided radiotherapy treatment planning. 2016;61(17):6531–52. https:\\doi.org\10.1088/0031-9155/61/17/6531

[58] Spadea MF, Maspero M, Zaffino P, Seco J. Deep learning based synthetic-CT generation in radiotherapy and PET: A review. 2021;48(11):6537–66. https:\\doi.org\10.1002/MP.15150

[59] AAPM Radiation Therapy Committee. Task Group No. 65., American Association of Physicists in Medicine. Tissue inhomogeneity corrections for megalovoltage photon beams: report of Task Group No. 65 of the Radiation Therapy Committee of the American Association of Physicists in Medicine. 2004;135.

[60] Zurl B, Tiefling R, Winkler P, Kindl P, Kapp KS. Hounsfield units variations: impact on CT-density based conversion tables and their effects on dose distribution. 2014;190(1):88–93. https:\\doi.org\10.1007/s00066-013-0464-5

[61] Snyder Karen C, Liu M, Zhao B, Huang Y, Ning W, Chetty IJ, et al. Investigating the dosimetric effects of grid size on dose calculation accuracy using volumetric modulated arc therapy in spine stereotactic radiosurgery. 2017;4(4):303–13.

[62] Koninklijke Philips N.V. 3D Geometric QA for research use. Vantaa, Finland; 2016.

[63] Teuho J, Linden J, Johansson J, Tuisku J, Tuokkola T, Teräs M. Tissue Probability-Based Attenuation Correction for Brain PET/MR by Using SPM8. 2016;63(5):2452–63. https:\\doi.org\10.1109/TNS.2015.2513064

[64] Dice LR. Measures of the Amount of Ecologic Association Between Species. 1945;26(3):297–302. https:\\doi.org\10.2307/1932409

[65] Menzel HG. The international commission on radiation units and measurements. 2010;10(1):1–106. https:\\doi.org\10.1093/jicru/ndq001

[66] Low DA, Harms WB, Mutic S, Purdy JA. A technique for the quantitative evaluation of dose distributions. 1998;25(5):656–61. https:\\doi.org\10.1118/1.598248

[67] Wang D, Strugnell W, Cowin G, Doddrell DM, Slaughter R. Geometric distortion in clinical MRI systems: Part I: Evaluation using a 3D phantom. 2004;22(9):1211–21. https:\\doi.org\10.1016/j.mri.2004.08.012

[68] Stanescu T, Jans H-S, Wachowicz K, Fallone BG. Investigation of a 3D system distortion correction method for MR images; Investigation of a 3D system distortion correction method for MR images. https:\\doi.org\10.1120/jacmp.v11i1.2961

[69] Sun J, Dowling J, Pichler P, Menk F, Rivest-Henault D, Lambert J, et al. MRI simulation: end-to-end testing for prostate radiation therapy using geometric pelvic MRI phantoms. 2015;60(8):3097–109. https:\\doi.org\10.1088/0031-9155/60/8/3097

[70] Korsholm ME, Waring LW, Edmund JM. A criterion for the reliable use of MRI-only radiotherapy. 2014;9(1). https:\\doi.org\10.1186/1748-717X-9-16

[71] Boukellouz W, Moussaoui A. Magnetic resonance-driven pseudo CT image using patch-based multi-modal feature extraction and ensemble learning with stacked generalisation. 2019; https:\\doi.org\10.1016/j.jksuci.2019.06.002

[72] Baran J, Chen Z, Sforazzini F, Ferris N, Jamadar S, Schmitt B, et al. Accurate hybrid template-based and MR-based attenuation correction using UTE images for simultaneous PET/MR brain imaging applications. 2018;18(1). https:\\doi.org\10.1186/s12880-018-0283-3

[73] Liney GP, Owen SC, Beaumont AKE, Lazar VR, Manton DJ, Beavis AW. Commissioning of a new wide-bore MRI scanner for radiotherapy planning of head and neck cancer. 2013;86(1027). https:\\doi.org\10.1259/bjr.20130150

[74] Chin AL, Lin A, Anamalayil S, Kevin Teo BK. Feasibility and limitations of bulk density assignment in MRI for head and neck IMRT treatment planning. 2014;15(5):100–11. https:\\doi.org\10.1120/jacmp.v15i5.4851

[75] Largent A, Marage L, Gicquiau I, Nunes JC, Reynaert N, Castelli J, et al. Head-and-Neck MRI-only radiotherapy treatment planning: From acquisition in treatment position to pseudo-CT generation. 2020;24(4):288–97. https:\\doi.org\10.1016/j.canrad.2020.01.008

[76] Lerner M, Medin J, Jamtheim Gustafsson C, Alkner S, Siversson C, Olsson LE. Clinical validation of a commercially available deep learning software for synthetic CT generation for brain. 2021;16(1):66. https:\\doi.org\10.1186/S13014-021-01794-6

[77] Gonzalez-Moya A, Dufreneix S, Ouyessad N, Guillerminet C, Autret D. Evaluation of a commercial synthetic computed tomography generation solution for magnetic resonance imaging-only radiotherapy. 2021;22(6):191. https:\\doi.org\10.1002/ACM2.13236

[78] Emami H, Dong M, Nejad-Davarani SP, Glide-Hurst CK. Generating synthetic CTs from magnetic resonance images using generative adversarial networks. 2018;45(8):3627–36. https:\\doi.org\https://doi.org/10.1002/mp.13047

[79] Liu X, Emami H, Nejad-Davarani SP, Morris E, Schultz L, Dong M, et al. Performance of deep learning synthetic CTs for MR-only brain radiation therapy. 2021;22(1):308–17. https:\\doi.org\10.1002/acm2.13139

[80] Wang H, Balter J, Cao Y. Patient-induced susceptibility effect on geometric distortion of clinical brain MRI for radiation treatment planning on a 3T scanner. 2013;58(3):465. https:\\doi.org\10.1088/0031-9155/58/3/465

[81] Jonsson JH, Akhtari MM, Karlsson MG, Johansson A, Asklund T, Nyholm T. Accuracy of inverse treatment planning on substitute CT images derived from MR data for brain lesions. 2015;10(1):1–7. https:\\doi.org\10.1186/s13014-014-0308-1

[82] Paradis E, Cao Y, Lawrence TS, Tsien C, Feng M, Vineberg K, et al. Assessing the dosimetric accuracy of magnetic resonance-generated synthetic CT images for focal brain VMAT radiation therapy. 2015;93(5):1154–61. https:\\doi.org\10.1016/j.ijrobp.2015.08.049

TURUN
YLIOPISTO
UNIVERSITY
OF TURKU